

Suprathermal electron spectra in the Venus ionosphere

J. Cui,^{1,2} M. Galand,² A. J. Coates,^{3,4} T. L. Zhang,^{5,6} and I. C. F. Müller-Wodarg²

Received 28 September 2010; revised 28 December 2010; accepted 9 February 2011; published 27 April 2011.

[1] In this study, a multistream kinetic model is used to derive the suprathermal electron intensity in the Venus ionosphere, to be compared with the observations made by the Analyzer of Space Plasmas and Energetic Atoms (ASPERA-4) Electron Spectrometer (ELS) instrument onboard Venus Express (VEx) on 18 May 2006. Input parameters of the model are chosen to be consistent with the detailed ephemeris information. We consider two cases for the magnetic field line configuration. The first assumes vertical magnetic field lines, while in the second the configuration is consistent with the VEx Magnetometer (MAG) measurements for that particular orbit. The model calculations suggest that the energy spectrum of suprathermal electrons not only depends on the local photoelectron production but is also strongly influenced by transport as well as energy degradation. We confirm the postulation of Coates et al. (2008) that the spectral features seen in the ASPERA-4 ELS data are signatures of O^+ (4S_0 , 2P_0 , and 2D_0) production by solar HeII 30.4 nm photons at altitudes where vertical transport is important. We also identify additional photoelectron peaks, in particular the peak associated with the ionization of atmospheric He by the solar HeII 30.4 nm photons. The combination of the identified photoelectron peaks provides a validation of the proposed spacecraft potential value of ~ -5 eV derived from the O^+ -related features by Coates et al. (2008). The model results indicate that the condition of local equilibrium is satisfied for suprathermal electrons below ~ 155 km on Venus. However, transport becomes effective at higher altitudes, significantly altering the secondary electron production rate and leading to strongly anisotropic suprathermal electron flow. For the case with the MAG-derived, slanted magnetic field configuration, we make a data-model comparison in terms of both the absolute magnitude of the suprathermal electron intensity and the appearance of spectral peaks. The comparison suggests that the actual magnetic field lines are probably inclined more vertically than a simple extrapolation from the MAG measurements.

Citation: Cui, J., M. Galand, A. J. Coates, T. L. Zhang, and I. C. F. Müller-Wodarg (2011), Suprathermal electron spectra in the Venus ionosphere, *J. Geophys. Res.*, *116*, A04321, doi:10.1029/2010JA016153.

1. Introduction

[2] Photoelectrons in planetary ionospheres, produced via ionization of ambient neutrals by solar EUV/X-ray radiation, serve as a significant source of ionization of neutrals and heating of thermal electrons [e.g., Fox et al., 2008]. A unique signature of photoelectrons is the presence of peak structures in the suprathermal electron spectra, associated with photo-

ionization of ambient atmospheric neutrals by the strong solar HeII 30.4 nm line, as well as other lines such as FeIX, X at 17.1 nm [e.g., Mantas and Hanson, 1979; Fox and Dalgarno, 1979]. The detection and identification of such peaks have been reported for measurements of suprathermal electron intensity in the sunlit ionosphere of Earth [e.g., Doering et al., 1976; Nagy et al., 1977; Solomon et al., 2001] and Titan [e.g., Galand et al., 2006; Coates et al., 2007; Robertson et al., 2009] associated with N_2 photoionization, and on Mars [e.g., Frahm et al., 2006a] and Venus [Coates et al., 2008, 2011] associated with CO_2/O photoionization. Similar spectral signatures associated with H_2 are also expected on Jovian planets [e.g., Waite et al., 1983; Galand et al., 2009]. The spectral features in the suprathermal electron energy spectrum have also been observed in distant regions where significant local photoionization is not expected, such as the terrestrial magnetosphere [Coates et al., 1985] and the darkside ionospheres or magnetospheric tail regions of Mars, Venus and Titan [e.g., Coates et al., 2007, 2011; Frahm et al., 2006b, 2010]. These observations imply a direct magnetic field line connection between the dayside planetary ionospheres and regions where the measurements were made.

¹National Astronomical Observatories, Chinese Academy of Sciences, Beijing, China.

²Space and Atmospheric Physics Group, Department of Physics, Imperial College, London, UK.

³Mullard Space Science Laboratory, University College London, Dorking, UK.

⁴Center for Planetary Sciences, University College London/Birkbeck, London, UK.

⁵Space Research Institute, Austrian Academy of Sciences, Graz, Austria.

⁶School of Earth and Space Sciences, University of Science and Technology of China, Hefei, China.

Therefore the suprathermal electron intensity can be used as a tracer of the magnetic field configuration in planetary environments [e.g., *Coates et al.*, 2011].

[3] Measurements of the suprathermal electron intensity at Venus have been obtained with the Retarding Potential Analyzer (RPA) onboard the Pioneer Venus Orbiter (PVO) [e.g., *Knudsen et al.*, 1980; *Knudsen and Miller*, 1985; *Spenner et al.*, 1980, 1996, 1997; *Szegő et al.*, 1997], though the energy resolution does not allow the photoelectron spectral peaks to be identified clearly. Along with these early PVO RPA in situ observations, various modeling efforts have been devoted into this topic [e.g., *McCormick et al.*, 1976; *Butler and Stolarski*, 1978; *Cravens et al.*, 1980; *Gan et al.*, 1990], mostly concentrated on the overall shape and magnitude of suprathermal electron spectrum as well as the associated thermal electron heating rate. More recently, the suprathermal electron intensity on Venus has been acquired from measurements made with the Electron Spectrometer (ELS) of the Analyzer of Space Plasmas and Energetic Atoms (ASPERA-4) onboard Venus Express (VEx) [*Barabash et al.*, 2007]. With a higher-energy resolution of $\Delta E/E \sim 7\%$ than that of the PVO RPA, distinct spectral peaks have been identified, and suggested as signatures of atomic O ionization (instead of CO₂) by solar HeII 30.4 nm photons at altitudes where vertical transport is expected to be important [*Coates et al.*, 2008]. However, such a postulation needs to be justified by a detailed model-data comparison.

[4] In this study, we investigate the suprathermal electron energy distribution in the Venus ionosphere based on a comparison of the VEx ASPERA-4 ELS observations with the output from kinetic model calculations. We assess in detail the interpretation of the spectral features in the observed suprathermal electron intensity, and identify regions of the Venus ionosphere where transport of the suprathermal electrons becomes important. The clear identification of the suprathermal electron peaks also provides an estimate of the VEx spacecraft potential [*Coates et al.*, 2008].

[5] The structure of the paper is as follows. The kinetic model and its input parameters adapted to Venus are described in section 2. The model results are presented in section 3 and compared with the VEx ASPERA-4 ELS data in section 4. Finally, we summarize our findings in section 5.

2. Model Description and Input Parameters

[6] We solve the suprathermal electron intensity, as a function of location along the magnetic field, energy and pitch angle (used to represent the angle between the velocity vector of the suprathermal electrons and the magnetic field vector, to be distinguished from the dip angle, used to represent the angle between the magnetic field vector and local horizontal) in the Venus ionosphere with a kinetic approach, based on the steady state Boltzmann equation,

$$\begin{aligned} \mu \frac{\partial \Phi_e}{\partial l} = & - \sum_n N_n \sigma_n^{(T)} \Phi_e + \frac{S}{4\pi} + N_e \frac{\partial}{\partial E} (L_e \Phi_e) \\ & + \sum_{n,k} N_n \sigma_n^{(k)} \int_{-1}^1 d\mu' \int_{E'>E} dE' R_n^{(k)} \Phi_e, \end{aligned} \quad (1)$$

where E is the suprathermal electron energy, l is the path length along the magnetic field line, μ is the cosine of the

pitch angle, $\Phi_e(l, E, \mu)$ is the suprathermal electron intensity (in units of $\text{cm}^{-2} \text{s}^{-1} \text{eV}^{-1} \text{sr}^{-1}$), $N_e(l)$ is the ambient thermal electron number density, $N_n(l)$ is the number density of ambient neutral species n , $\sigma_n^{(T)}(E)$ is the total electron impact cross section for species n , $S(l, E)$ is the primary photoelectron production source function (in units of $\text{cm}^{-3} \text{s}^{-1} \text{eV}^{-1}$) assumed to be isotropic, $L_e(E)$ is the electron stopping cross section (in units of $\text{cm}^2 \text{eV}$) used to parametrize the inelastic Coulomb collisions between suprathermal and thermal electrons, $\sigma_n^{(k)}(E)$ is the electron impact cross section for species n and process k , $R_n^{(k)}(E', \mu' \rightarrow E, \mu)$ is the corresponding energy and angular redistribution function.

[7] While the left hand side of equation (1) gives the change in suprathermal electron intensity with the path length l due to transport, the terms on the right hand side represent (1) loss of suprathermal electrons at (l, E, μ) through collisions with ambient neutrals; (2) primary photoelectron production by absorption of solar flux (described with the Beer-Lambert law); (3) forward scattering of suprathermal electrons through Coulomb collisions with ambient thermal electrons; and (4) the redistribution of high-energy electrons to lower energies through inelastic collisions with ambient neutrals. The effect of impact ionization by suprathermal electrons (i.e., secondary electron production) is taken into account by the last term of equation (1). The contribution of magnetospheric electrons is ignored in the model, since the PVO RPA measurements of suprathermal electrons on Venus suggest a dominant solar radiation origin at the dayside [e.g., *Knudsen et al.*, 1980].

[8] Equation (1) is solved with a multistream scheme (here 16 streams) to obtain the angular distribution of the suprathermal electron energy spectrum. The energy grid is defined to be roughly log linear with a total number of 340 intervals from 10 eV to 3 keV. The full spherical nature of the Venus atmosphere is taken into account. The kinetic model outlined above has been successfully applied to previous investigations of the suprathermal electron population in the ionospheres of other Solar System bodies, such as Titan [*Galand et al.*, 2006] and Saturn [*Galand et al.*, 2009; *Moore et al.*, 2008]. Information on the electron stopping cross section, L_e , as well as the angular and energy redistribution function, $R_n^{(k)}$, can be found in these references. The various photon impact and electron impact cross sections used for the present study, which have been updated from the previous model, are described in Appendix A.

[9] The incident solar EUV/X-ray flux is based on the information acquired with the Solar EUV Experiment (SEE) instrument of the NASA Thermosphere Ionosphere Mesosphere Energetics and Dynamics (TIMED) mission [*Woods et al.*, 2005], scaled to the value at Venus. We adopt the SEE level 3 measurements for wavelength range between 40 and 100 nm, with a resolution of 1 nm. Below 40 nm, the SEE level 4 modeled solar irradiance data, constructed on a wavelength grid of width 0.1 nm, are used. We scale the SEE level 4 solar spectrum by requiring that below 40 nm, the level 4 model irradiance integrated over each 1 nm interval be identical to the corresponding level 3 value.

[10] The Venus neutral atmosphere model used for this study is shown in Figure 1, including 8 atomic and molecular species (CO₂, CO, O, N₂, N, H₂, H and He). The density profiles of CO₂, CO, N₂, O, N and He are taken from the VTS3 model [*Hedin et al.*, 1983] between 100 and 600 km

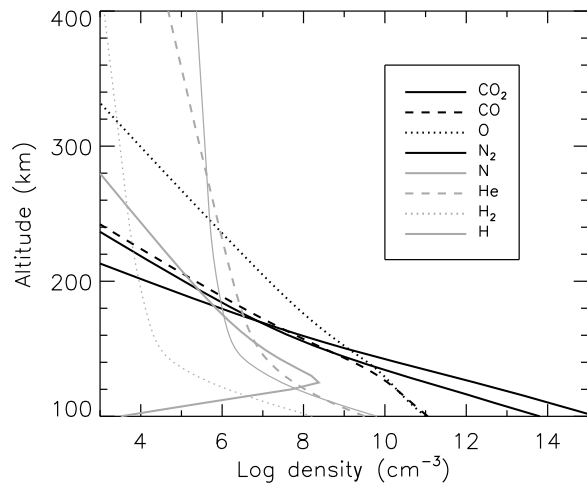


Figure 1. Venus neutral atmosphere model used for the kinetic calculations. The densities of CO₂, CO, O, N₂, N, and He are taken from *Hedin et al.* [1983] for solar minimum conditions and for a latitude of 85°N. The profiles of H₂ and H are derived by assuming diffusive equilibrium, following the procedures of *Fox and Sung* [2001].

altitude. The distributions of H₂ and H are calculated with the diffusive equilibrium approximation (i.e., assuming zero H and H₂ diffusion fluxes) following the scheme of *Fox and Sung* [2001]. While H₂ is always a minor species throughout the altitude range considered in this work, we note that the distribution of H is important to our numerical solution above ~300 km where it becomes the dominant species according to Figure 1. However, such an atomic H distribution should be

regarded as an upper limit: If strong H escape is present on Venus [e.g., *Hartle et al.*, 1996], the H densities at high altitudes may be significantly reduced, making He the dominant species there. In sections 3 and 4, we will present both results based on the neutral atmosphere model with and without H. For the other neutral species ignored in our model, NO is the only one that may contribute appreciably to the derived suprathermal electron intensity, for altitudes near or below the Venus ionospheric peak at ~140–150 km [e.g., *Cravens et al.*, 1981; *Fox*, 2007]. This is because NO has a relatively low ionization threshold of 9.3 eV [*Reiser et al.*, 1988], as compared with 13.8 eV for CO₂ [*Gustafsson et al.*, 1978] and 13.6 eV for O [*Tayal*, 2002]. Despite this, it is justified to ignore NO here since we are mainly interested in regions of the Venus ionosphere well above the ionospheric peak due to the availability of existing VEx data. Indeed, NO primarily influences the suprathermal electron spectra in regions of the Venus ionosphere where local equilibrium roughly holds, whereas the VEx observations were made at higher altitudes where transport becomes dominant (see sections 3 and 4). For the thermal electron density and temperature profiles required by the model calculations, we do not choose to calculate them in a self-consistent manner. Instead, they are directly taken from the empirical results of *Theis et al.* [1984], based on the PVO Electron Temperature Probe (ETP) data obtained from December 1978 to December 1982. This is a reasonable approach since in this study we are mainly interested in ionizing processes above 10 eV.

[11] The input parameters of the kinetic model are chosen to be consistent with the ephemeris and VEx trajectory information on 18 May 2006 [*Coates et al.*, 2008], as shown in Figure 2 (left). The TIMED/SEE spectrum averaged over

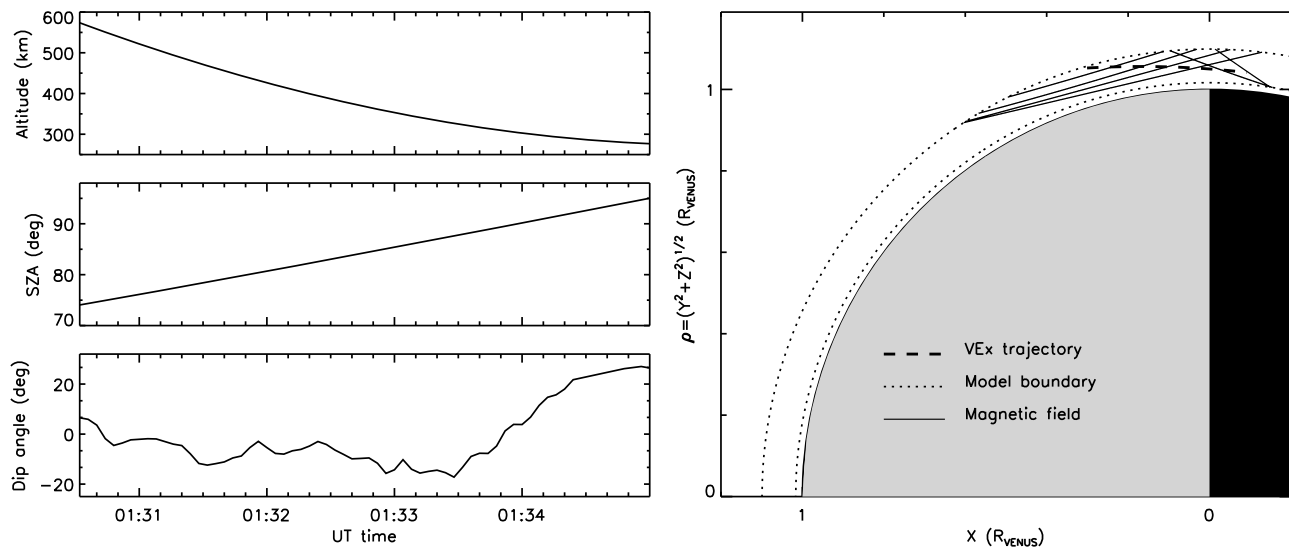


Figure 2. (left) Ephemeris and VEx trajectory information (including altitude, solar zenith angle, and magnetic field dip angle) for the 18 May 2006 observation reported by *Coates et al.* [2008]. Suprathermal electron spectra of ionospheric origin were obtained for the portion of the VEx orbit shown (0130:32–0135:00 UT). (right) The portion of the VEx orbit considered in this study (solid line), as well as the model upper and lower boundaries (dotted lines), plotted in Venus Solar Orbital (VSO) coordinates (in units of Venus radius), with the Sun to the left. The magnetic field configuration is also drawn at several representative locations along the VEx orbit, assuming a constant magnetic field direction for each field line (solid line).

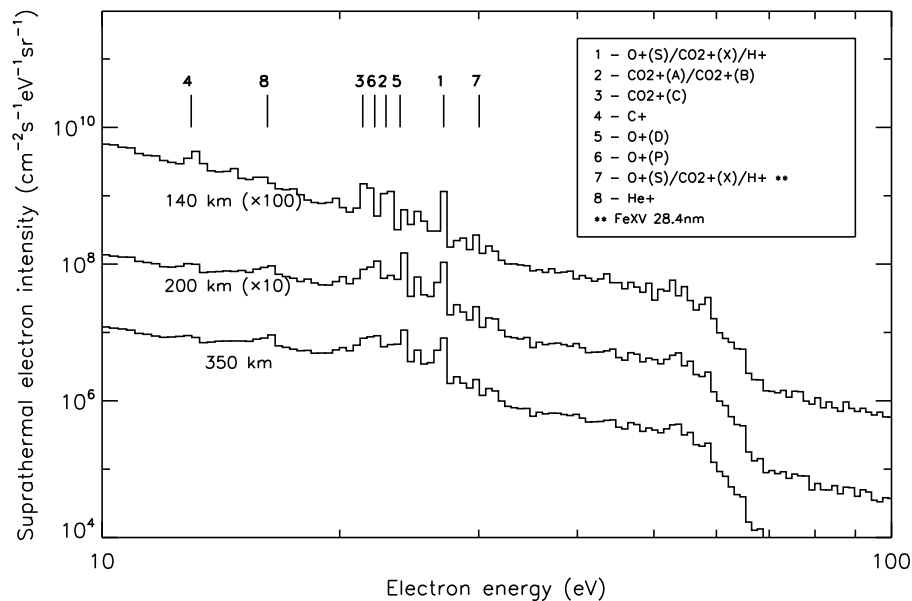


Figure 3. The model suprathermal electron intensity averaged over solid angle for several representative altitudes. The intensities at 200 and 350 km have been multiplied by 10 and 100, respectively, to improve visibility. Several spectral features have been identified, marked by the vertical bars and with notation given in the box (see also Table 1). All features are associated with the ionization of ambient neutrals in the Venus upper atmosphere by solar HeII 30.4 nm photons, except for feature 7 (marked with two asterisks) which is associated with ionization by solar FeXV 28.4 nm photons.

the same day is used, corresponding to a solar index of $F10.7 = 73$. The suprathermal electron spectrum of day-side ionospheric origin was obtained during the 0130:32–0135:00 UT period near the north pole of Venus, with solar zenith angle in the range of $\sim 75^\circ$ – 95° [Coates *et al.*, 2008]. Accordingly, the average VTS3 densities at a latitude of 85°N , averaged over local time, and under solar minimum conditions, are used for constructing the Venus neutral background model shown in Figure 1. The corresponding altitude range of ~ 280 – 570 km along the spacecraft trajectory is well within the model boundaries of 100–600 km. Note that the periapsis is slightly above the Venus ionopause at ~ 250 km for solar minimum conditions [e.g., Zhang *et al.*, 2008].

[12] The choice for the magnetic field configuration determines how the suprathermal electrons are transported. Here we consider two cases. First, we assume vertical magnetic field lines in the region of our interest, corresponding to the extreme situation in which suprathermal electrons can be transported from the deepest region of the Venus ionosphere. However, this is an idealistic case compared to the actual situation due to the known draped nature of the magnetic field configuration near Venus [e.g., Luhmann and Cravens, 1991]. This is shown in the bottom panel of Figure 2 (left) with the magnetic field dip angle along the VEx spacecraft trajectory based on the simultaneous VEx Magnetometer (MAG) data [e.g., Zhang *et al.*, 2006]. Therefore in the second case, we adopt the measured magnetic field configuration by assuming a constant magnetic field direction. This is justified because the magnetic field is not expected to change significantly over scales much smaller than the planetary radius, except near the bow shock [e.g., Slavin *et al.*, 1980]. The magnetic field lines are plotted in Figure 2 (right) in

Venus Solar Orbital (VSO) coordinates [e.g., Coates *et al.*, 2008], for several representative locations along the VEx orbit. Variations of solar zenith angle along the adopted magnetic field lines are taken into account when solving equation (1). The model upper and lower boundaries of 100 and 600 km are also indicated in Figure 2 (right), in units of Venus radius (6052 km).

3. Characteristics of Suprathermal Electron Intensity in the Venus Ionosphere

[13] In this section, we show results from our kinetic model described in section 2. Here we focus on the case for vertical magnetic field lines, and leave discussions of the MAG-derived magnetic field case until section 4, where we compare the model results with the ASPERA-4 ELS data. Both cases share similar underlying physics.

3.1. Photoelectron Spectral Features

[14] We present in Figure 3 the suprathermal electron intensities averaged over solid angle, as a function of energy, for several representative altitudes (140, 200 and 350 km). The intensities at 140 and 200 km have been multiplied by 100 and 10, respectively, to improve visibility. A sharp decrease in electron spectrum is seen near ~ 63 eV, which is caused by the drop in solar flux at ~ 16 nm (i.e., ~ 77 eV) with the corresponding shift of ~ 14 eV being the typical value of ionization threshold of neutral species in the Venus atmosphere. This feature is also seen at other Solar System bodies, such as Earth [Lee *et al.*, 1980] and Titan [Galand *et al.*, 2006].

[15] A number of spectral features are identified in Figure 3, marked by vertical bars at the top. These features

Table 1. Summary of the Spectral Features Identified in the Calculated Suprathermal Electron Energy Spectrum in the Venus Ionosphere^a

Feature Number	Solar Line	Ionization Process	E_{th} (eV)	E_e (eV)
1	HeII 30.4 nm	$O \rightarrow O^+(^4S_0)$	13.62	27.2
		$CO_2 \rightarrow CO_2^+(X^2\Pi_g)$	13.79	27.0
		H^+	13.60	27.2
2	HeII 30.4 nm	$CO_2 \rightarrow CO_2^+(A^2\Pi_u)$	17.72	23.1
		$CO_2 \rightarrow CO_2^+(B^2\Sigma_u^+)$	18.08	22.7
3	HeII 30.4 nm	$CO_2 \rightarrow CO_2^+(C^2\Sigma_g^+)$	19.40	21.4
4	HeII 30.4 nm	$CO_2 \rightarrow C^+ + \text{neutrals}$	27.82	13.0
5	HeII 30.4 nm	$O \rightarrow O^+(^2D_0)$	16.94	23.8
6	HeII 30.4 nm	$O \rightarrow O^+(^2P_0)$	18.64	22.1
7	FeXV 28.4 nm	$O \rightarrow O^+(^4S_0)$	13.62	30.1
		$CO_2 \rightarrow CO_2^+(X^2\Pi_g)$	13.79	29.9
		H^+	13.60	30.1
8	HeII 30.4 nm	$He \rightarrow He^+$	24.59	16.2

^aSee also Figure 3. E_{th} and E_e represent ionization threshold and photoelectron energy, respectively.

are produced via photoionization of various neutral species in the ambient atmosphere by strong solar lines, especially the HeII 30.4 nm line. In the Venus atmosphere, the most abundant neutral species is CO_2 below ~ 150 km, H/He above ~ 240 km, and O between (see Figure 1). Therefore we expect all these species to produce signatures in the suprathermal electron energy distribution. The main spectral features identified in Figure 3 are listed in Table 1, including the corresponding solar lines, the ionization process, the threshold energy, as well as the photoelectron energy. Ionization channels to different excited electronic states of CO_2 and O have been included. Most of the spectral features are associated with photoionization by the solar HeII 30.4 nm line. However, one signature representing $O^+(^4S_0)$, $CO_2^+(X^2\Pi_g)$ and/or H^+ production by the solar FeXV 28.4 nm line (labeled as feature 7 in Figure 3 and Table 1) is also clearly apparent. We can also see the spectral peak at ~ 59 eV (not labeled in Figure 3) associated with the ionization of the same atomic species by the FeIX, X photons at 17.1 nm. As mentioned in section 2, the atomic H density profile is calculated by assuming diffusive equilibrium, which might be an overestimate in case of strong H escape on Venus. However, the presence of the H^+ signature (in features 1 and 7) is not critically dependent on this assumption, since the model calculations with H excluded from the neutral background atmosphere gives very similar suprathermal electron energy spectra at all altitudes. This indicates that features 1 and 7 are primarily contributed by $O^+(^4S_0)$ and $CO_2^+(X^2\Pi_g)$ for the case with vertical magnetic field lines. Note that this may not be true for the MAG-derived, slanted magnetic field orientation (see section 4 for details). Due to the finite energy resolution adopted for the numerical calculations, different ionization processes do not always appear as distinct peaks in the suprathermal electron energy spectrum. For example, the $CO_2^+(A^2\Pi_u)$ and $CO_2^+(B^2\Sigma_u^+)$ features, separated by ~ 0.4 eV, are blended in the model spectrum (feature 2 in Figure 3 and Table 1). This is also true for the $O^+(^4S_0)$, $CO_2^+(X^2\Pi_g)$ and H^+ features, separated by ~ 0.2 eV (feature 1 in Figure 3 and Table 1). However, H^+ can be distinguished from O^+ and CO_2^+ through the presence (or lack thereof) of spectral features due to the excited states of these two ion species. Since the

wavelength resolution of the solar flux is 0.1 nm, higher resolution in the model suprathermal electron flux is not justified.

[16] The altitude evolution of the spectral features clearly reflects the distribution of neutral constituents in the ambient atmosphere. For example, the photoelectron peak associated with C^+ production is more prominent at low altitudes, in response to the variation of the relative abundance of CO_2 with altitude. This spectral peak is indicated by feature 4 in Figure 3. With the similar line of reasoning, we can explain the variation of the He^+ peak (feature 8) with altitude, as well as the nonmonotonic variation of the $O^+(^2D_0)$ peak (feature 5) with altitude, in accordance with the atomic O density distribution on Venus [Hedin *et al.*, 1983]. Figure 3 shows the presence of a local maximum near 22–24 eV at all altitudes, which includes features 2, 3, 5 and 6. Close examination, however, shows that it is associated with the two excited states of O^+ (5, 6) at 200 and 350 km and with the two excited states of CO_2^+ (2, 3) at 140 km. We have tested this by artificially changing the O ionization threshold and running the kinetic model again to see if features 5 and 6 are shifted to the expected energies. The association of the 22–24 eV local maximum with different neutral species is clearly a result of CO_2 dominance at low altitudes but O dominance above. Here it is also interesting to note the difference between Venus and Mars in the interpretation of photoelectron peaks, due to their different neutral atmospheric structures. For Mars, the relatively small O-to- CO_2 density ratio leads to a CO_2 column photoionization rate nearly 10 times higher than that for O [e.g., Fox and Dalgarno, 1979]. This implies that even well above the ionospheric peak, the 22–24 eV photoelectron signature observed at Mars is primarily due to ionization of CO_2 rather than of O [Frahm *et al.*, 2006a; Haider *et al.*, 2010].

3.2. Effect of Transport

[17] The above analysis shows that the appearance of spectral features in suprathermal electron intensity is, at least partly, determined by the dominant ion production at a given altitude [Coates *et al.*, 2008]. Another factor determining the electron energy distribution as a function of altitude is transport, as suggested by Coates *et al.* [2008] in their initial interpretation of the ASPERA-4 ELS data.

[18] To illustrate the role of transport, we compare various terms of equation (1) (integrated over solid angle) in Figure 4, as a function of altitude for a reference suprathermal electron energy of 20 eV. The solid, dashed, dotted and dash-dotted lines represent the effects of transport, primary production, collision with neutrals, and Coulomb collision with thermal electrons, respectively. Positive and negative signs in Figure 4 stand for production and loss, respectively. At 20 eV, Coulomb collision with thermal electrons is insignificant except above ~ 250 km. This implies that possible uncertainties in the thermal electron model (see section 2) do not have an appreciable effect on our results. However, it may become important for the particle balance of low-energy suprathermal electrons. The region below ~ 155 km is characterized by local equilibrium, where the contribution of transport is small and primary photoelectron production at a given energy is closely balanced by loss of suprathermal electrons at that energy by collisions with ambient neutrals.

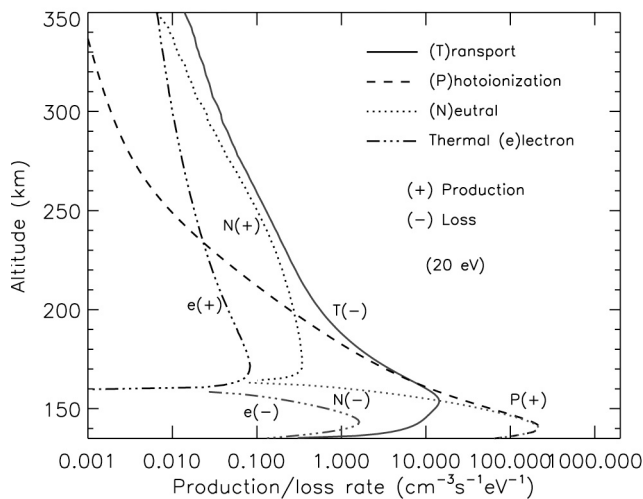


Figure 4. A comparison between various terms of the Boltzmann equation (equation (1)) as a function of altitude and for a reference electron energy of 20 eV. The region below ~ 155 km is characterized by local equilibrium for suprathermal electrons, and the effect of transport becomes important above. Above ~ 250 km, loss of suprathermal electrons through transport is primarily balanced by production through collision with ambient neutrals.

Above ~ 250 km, primary production is negligible and loss through transport is balanced by production through neutral collisions. A broad transition region of ~ 100 km width lies between the local equilibrium region and the transport controlled region. Figure 4 also reveals that below ~ 165 km, downward cascade from $E = 20$ eV to $E < 20$ eV is more important than that from $E > 20$ eV to $E = 20$ eV. However, such an effect reverses sign at higher altitudes, indicating that downward cascade from $E > 20$ eV to $E = 20$ eV becomes more important than that from $E = 20$ eV to $E < 20$ eV. The collision term reverses sign at ~ 165 km. Below this altitude, downward cascade from 20 eV to lower energies is more effective than that from higher energies to 20 eV, while it is less effective above that altitude. A similar transition region from local equilibrium to transport dominance has been found in previous model calculations of the suprathermal electron population in the Venus ionosphere [e.g., *Cravens et al.*, 1980], though the exact location of the transition region varies with the adopted input parameters.

[19] Transport also affects secondary electron production in the Venus ionosphere. This is illustrated in Figure 5, where we compare the altitude profiles of primary production and secondary production with/without transport. The secondary production rate is not affected by transport below ~ 160 km, consistent with the region of local equilibrium for 20 eV suprathermal electrons (see Figure 4). Between ~ 160 and ~ 320 km, ignoring transport overestimates the secondary electron production rate by an average factor of ~ 3 . However, at higher altitudes, ignoring transport underestimates the secondary electron production rate by an average factor of $\sim 50\%$. It is interesting to note that the effect of transport on secondary electron production rate relies on the adopted H density profile for solving equation (1). In addition to the nominal choice of atomic H distribution in diffusive equi-

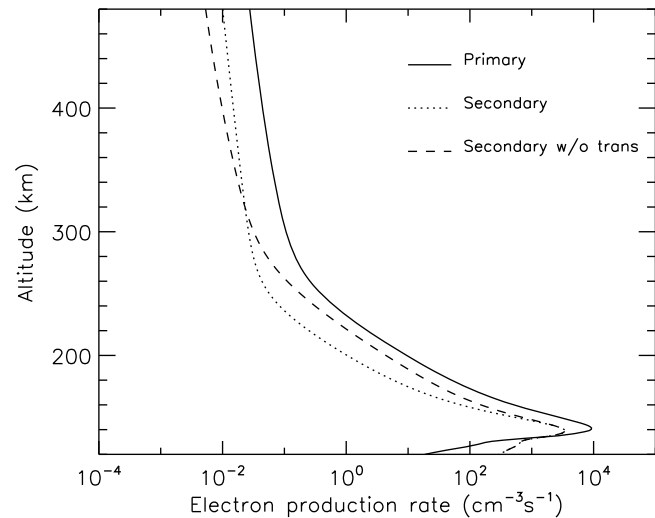


Figure 5. The secondary electron production rates with and without transport as a function of altitude in the Venus ionosphere, calculated from our kinetic model. Also shown is the primary electron production rate in the same altitude range. The effect of transport on secondary production is clear above ~ 160 km.

librium, we make test runs with H taken out, representing the extreme case of strong H escape from Venus. In this case, the secondary electron production rate obtained with transport taken out is always an overestimate compared with the case including transport, as shown in Figure 6.

[20] Normally, when primary production is important, ignoring transport tends to enhance local electron impact ionization, since more photoelectrons are available for producing secondary electrons. This explains the enhanced secondary electron production rate below ~ 320 km for the

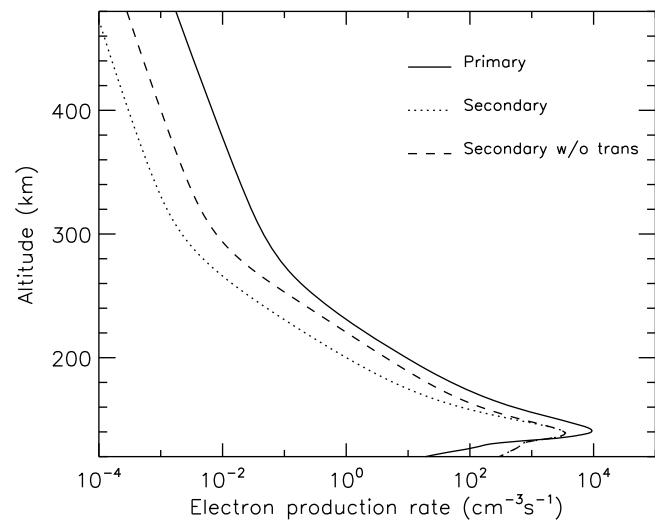


Figure 6. The same as Figure 5 but for the case with H taken out of the model. This represents the case with strong H escape on Venus, and He becomes the dominant neutral species above ~ 240 km. In this case, ignoring the effect of transport causes an overestimate of the secondary electron production rate above ~ 160 km.

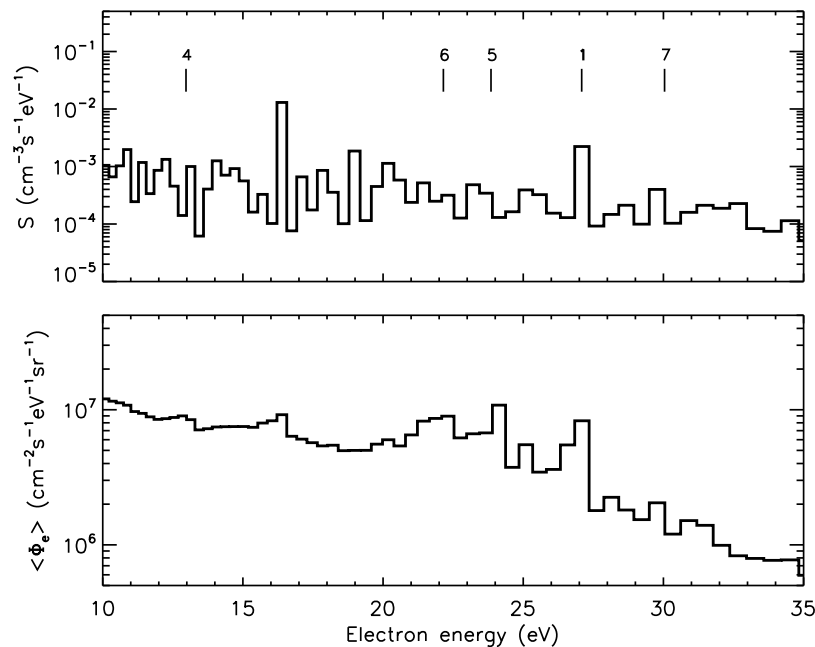


Figure 7. (top) The primary production source function and (bottom) the suprathermal electron intensity (averaged over solid angle) as a function of electron energy at 300 km in the Venus ionosphere. At low energies, the complex structure in the primary production source function is effectively “washed out” by energy degradation and no longer seen in the suprathermal electron intensity.

case both with and without H. In contrast, at high altitudes where primary production is negligible and transport is ignored, the particle budget for suprathermal electrons is characterized by a balance between collision with neutrals and collision with thermal electrons. Accordingly, the secondary electron production rate is limited by Coulomb collisions instead of primary production. For the case with H, the photoelectron energy is on average greater than that for the case without H, due to the relatively low ionization threshold for H compared with He. Since the stopping cross section increases with decreasing energy, the Coulomb collision rate, and accordingly the neutral collision rate, is lower for the case with H as compared to the case without H. This fact leads to the distinct behaviors of secondary electron production for the two cases above ~ 320 km as shown in Figures 5 and 6. Finally, we note that in terms of total electron production rate, transport of photoelectrons (and their secondaries) is not important near or above the ionospheric peak, as in this region photoionization is always the dominant ionizing process.

3.3. Effect of Energy Degradation

[21] The suprathermal electron spectrum is also modified by energy degradation. This is illustrated in Figure 7, where we compare the primary production source function (top) and suprathermal electron intensity averaged over solid angle (bottom) at 350 km. Several prominent spectral features are labeled in Figure 7 following the convention of Figure 3. In Figure 7, complex structures are seen below ~ 15 eV, interpreted by photoionization of various ambient neutrals. However, except for the weak structure at ~ 13 eV associated with C^+ production (feature 4), the suprathermal electron intensity below ~ 15 eV appears to be very smooth. This is interpreted as a result of energy degradation.

[22] The overall effect of inelastic collisions with ambient neutrals and thermal electrons is to steepen the slope as well as to smooth the shape of the suprathermal electron spectrum. When the smoothing effect induced by energy degradation is large, spectral features resulting from photoionization may no longer be seen. The electron impact cross sections for various inelastic processes typically increase with decreasing energy well above the threshold, implying that energy degradation is more efficient for low-energy electrons. This explains why the low-energy signatures are smeared out while those at higher energies survive. Since the inelastic collision frequency is proportional to the local densities of neutrals or thermal electrons, energy degradation is more effective at relatively low altitudes. This can be seen from the fact that the shape of the suprathermal electron spectrum becomes steeper in deeper regions of the ionosphere (see Figure 3). More specifically, the average value of $-d \log \langle \Phi_e \rangle / d \log E$ below 50 eV is ~ 3 near the ionospheric peak, but drops to a constant level of ~ 2.2 – 2.3 above 250 km, where $\langle \Phi_e \rangle$ is the suprathermal electron intensity averaged over solid angle.

[23] Figure 7 also illustrates the importance of transport, through the clear presence of spectral features 5 and 6 (associated with the production of two excited states of O^+ , see Table 1) in the suprathermal electron intensity. In contrast, these features are not obvious in the corresponding source function, since the ambient O densities are relatively small at such high altitudes. Therefore we interpret the presence of features 5 and 6 at 350 km as a result of transport rather than local production, confirming the suggestion of Coates *et al.* [2008].

[24] Finally, we show in Figure 8 information on the anisotropy of suprathermal electron flow in the Venus ionosphere, based on our multistream model calculations. Figure 8 (left) gives the projected upward (Φ_e^+) and downward

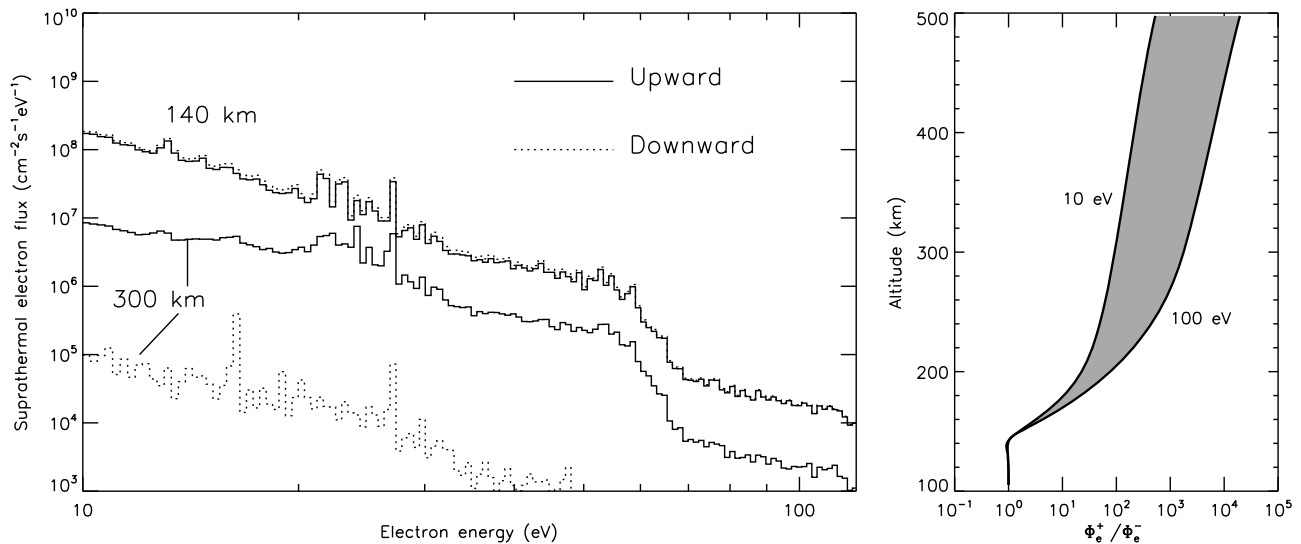


Figure 8. (left) The projected upward (Φ_e^+) and downward (Φ_e^-) suprathermal electron flux densities as a function of energy at 140 and 300 km, respectively. Near or below the ionospheric peak, the suprathermal electron flow is nearly isotropic. At 300 km, the electron flow becomes highly anisotropic. (right) The ratio between the upward and downward suprathermal electron flux densities as a function of altitude and for different levels of electron energy. Anisotropy starts to be important above ~ 140 km.

(Φ_e^-) flux densities as a function of electron energy at 140 and 300 km, respectively. The electron flow is roughly isotropic near or below the ionospheric peak, corresponding to a region where the electron energy is lost locally. At 300 km, the downward flux is significantly lower than the upward flux at all energies, causing strong anisotropic suprathermal electron flow. We show the ratio between the upward and downward suprathermal electron flux densities as a function of altitude in Figure 8 (right), with the shadowed region encompassing the electron energy range of 10–100 eV. The transition between isotropic and anisotropic flow occurs at about the same altitude where local equilibrium for suprathermal electrons starts to break down (see Figure 4) and secondary electron production starts to be significantly affected by transport (see Figure 5). We can also see from Figure 8 that more energetic electrons present a higher degree of anisotropic transport, due to their small collision cross section and small angular redistribution function as compared with low-energy electrons.

4. Data-Model Comparison

[25] In this section, we compare the model results with the VEx ASPERA-4 ELS measurements reported by *Coates et al.* [2008]. The early PVO RPA results will not be investigated here since the energy resolution does not allow prominent photoelectron peaks to be identified clearly [e.g., *Knudsen et al.*, 1980]. The resolution of the ASPERA-4 ELS data is $\Delta E/E \sim 7\%$ [Coates et al., 2008], corresponding to ~ 2 eV near 25 eV. Therefore the quadruplet structure near 23 eV (features 2, 3, 5 and 6 in Figure 3) appears as two doublets, one associated with $\text{CO}_2^+(\text{A}^2\Pi_u, \text{B}^2\Sigma_u^+)$ and $\text{O}^+(\text{D}_0)$ production, and the other one associated with $\text{CO}_2^+(\text{C}^2\Sigma_g^+)$ and $\text{O}^+(\text{P}_0)$ production. The observed suprathermal electron spectrum is shifted relative to the model spectrum due to the VEx spacecraft potential, which we estimate to be ~ -5 eV by

the positions of the photoelectron peaks associated with He^+ and the three excited states of O^+ . This confirms the value reported by *Coates et al.* [2008], derived from the O^+ -related photoelectron peaks.

[26] A detailed comparison in suprathermal electron energy spectrum between the model results and the ASPERA-4 ELS data (corrected for spacecraft potential) is given in Figure 9 for the case of vertical magnetic field configuration. The comparison in suprathermal electron intensity for a given pitch angle will be presented below for the case with the MAG-derived, slanted magnetic field lines. In Figure 9, the observed spectrum is the average result of 10 consecutive 4 s samples obtained at 0134:20–0135:00 UT and at an altitude of ~ 459 km. Only ELS anode 11, which is unaffected by instrument obscuration, is used for the comparison. The model spectrum is obtained at the same altitude, with the transport term included in equation (1). Figure 9 shows that the model spectrum is consistent with the data in terms of the presence of spectral peaks (as labeled with the drawing convention of Figure 3). The absolute magnitude of the calculated suprathermal electron intensity, however, is significantly overestimated. Such a disagreement can be caused by the uncertainties in the Venus neutral atmosphere model and/or the ambient magnetic field configuration, as well as the contribution from energetic electrons from the solar wind or the induced magnetosphere of Venus that has not been included in our model calculations.

[27] The Venus neutral atmospheric structure adopted in our calculations is based on the VTS3 model [Hedin et al., 1983], constructed from the PVO neutral mass spectrometer measurements made at altitudes above 150 km near latitude 16°N for solar maximum conditions [Hedin et al., 1983], thus an extrapolation to low solar activity conditions and polar regions (appropriate to the VEx data) should be taken with caution. Initial results from the VEx Atmospheric Drag Experiment (ADE) suggest that polar mass densities near

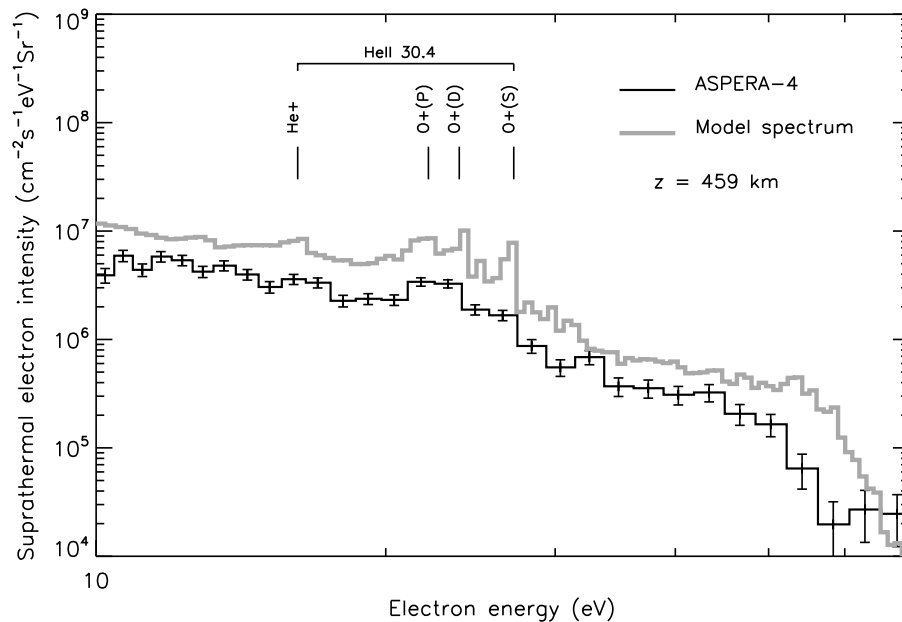


Figure 9. A comparison in suprathermal electron intensity between the model calculations and the 18 May 2006 ASPERA-4 ELS data obtained at ~ 459 km and for a pitch angle of 143° . The data are given by the black histogram (with error bars). The model is given by the solid gray histogram and has been averaged over solid angle. A vertical magnetic field configuration is assumed in the calculations.

175–185 km at solar minimum may be around a factor of 2.5 lower than those predicted for the same location and condition by VTS3 (P. Rosenblatt et al., First ever in situ observations of Venus’ polar upper atmosphere density using the tracking data of the Venus Express Atmospheric Drag Experiment (VExADE), submitted to *Icarus*, 2010). Unfortunately, there is no mass spectrometer onboard VEx, thus the densities of individual neutral species are not measured. This makes it difficult to evaluate accurately how the derived suprathermal electron spectra may be affected by uncertainties in the neutral atmosphere model. An additional uncertainty in the neutral atmosphere model is the possible presence of a hot O corona at Venus [e.g., Nagy et al., 1981; Nagy and Cravens, 1988; Hodges, 2000]. While this may affect the appearance of the O related peaks in our model spectra, we do not expect the absolute magnitude of suprathermal electron intensity to be influenced appreciably, due to the low density of hot O atoms [e.g., Lichtenegger et al., 2009].

[28] As discussed in section 2, the model results also depend critically on the adopted magnetic field configuration, since this determines how suprathermal electrons are transported. The data-model comparison presented in Figure 9 is based on the assumption of vertical magnetic field lines, which is an extreme case. The magnetic field lines near Venus are expected to drape around the planet [e.g., Luhmann and Cravens, 1991]. The local magnetic field orientation and strength have been obtained by the MAG instrument along the VEx trajectories. These measurements are used to extract the entire magnetic field configuration in our region of interest (see section 2 for details). The corresponding data-model comparison at 306 km is presented in Figure 10. To take into account the anisotropy in suprathermal electron intensity, we choose a pitch angle of 143° , appropriate for ELS anode 11 and associated with an outward flow. The correspond-

ing magnetic field dip angle is 17° at that altitude. Figure 10 shows that, for the case with VEx MAG-derived, slanted magnetic field configuration, the agreement in the absolute magnitude of the electron energy spectrum is significantly improved over the vertical magnetic field case, with the agreement between 15 and 50 eV on average better than 20%. However, the suprathermal electron spectrum seems to be underestimated below ~ 15 eV. The disagreement cannot be due to the high-energy tail of the thermal electron population not included in our calculations, which is negligibly small at the energies considered here. The suprathermal electron fluxes at low energies are largely controlled by energy degradation of higher-energy electrons by collisions with ambient neutral particles. Therefore we expect the disagreement below ~ 15 eV to be related to the uncertainties in the neutral atmosphere model.

[29] Although Figure 10 shows consistency between the calculated and the measured electron fluxes, the model cannot be extrapolated to other altitudes. We find that at relatively high altitudes, the model spectrum tends to be significantly lower than the observations. An example is given in Figure 11 for a comparison made at ~ 459 km and with the same pitch angle of 143° associated with an outward flow. The corresponding magnetic field dip angle is 8° . The apparent difference in the absolute magnitude of the suprathermal electron intensity, by a factor of nearly an order of magnitude, is probably too large to be associated with uncertainties in the neutral atmosphere model. However, this could be produced by an overdamped magnetic field line configuration, since more suprathermal electrons can be produced through primary and secondary production as the magnetic field lines are inclined more vertically. This argument is reinforced further by the appearance of spectral peaks in at least two aspects. First, the calculated spectral peaks tend to be more visible

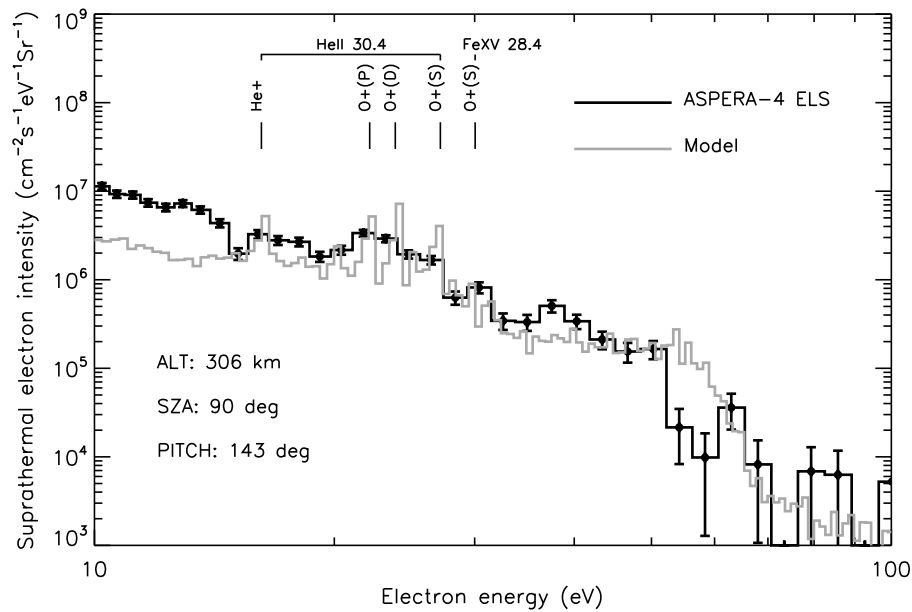


Figure 10. A comparison in suprathermal electron intensity between the model calculations and the ASPERA-4 ELS data obtained at ~ 306 km on 18 May 2006. Only ELS anode 11 is used to avoid possible obscuration effects. The data are given by the black histogram (with error bars), and the model is given by the gray histogram, with the effect of transport taken into account. A slanted magnetic field configuration is assumed in the calculations, based on the VEx MAG measurements assuming constant magnetic field orientation.

than the observed ones, implying that not enough collisions are included in the model calculations to smooth them. Secondly, and more importantly, the model spectrum does not present signatures of $O^+(^2D_0)$ and $O^+(^2P_0)$ states which are clearly seen in the data. In addition, in the model spectrum, the strong spectral peak near 27 eV is formed by the production of H^+ instead of $O^+(^4S_0)$, as labeled in Figure 11. Similarly, the model peak near 30 eV is associated with H^+ production by the FeXV 28.4 nm photons. These facts imply

that the location under study is not magnetically connected to deep regions of the Venus atmosphere where the atomic O ionization can be significant. In contrast, for the case with vertical magnetic field lines connecting the high altitude to the low-altitude regions, the spectral peaks associated with O ionization are clearly identified in the model spectrum at 459 km due to vertical transport of electrons (see Figure 9).

[30] In a similar manner, data-model comparisons have been made at other altitudes, and help to provide con-

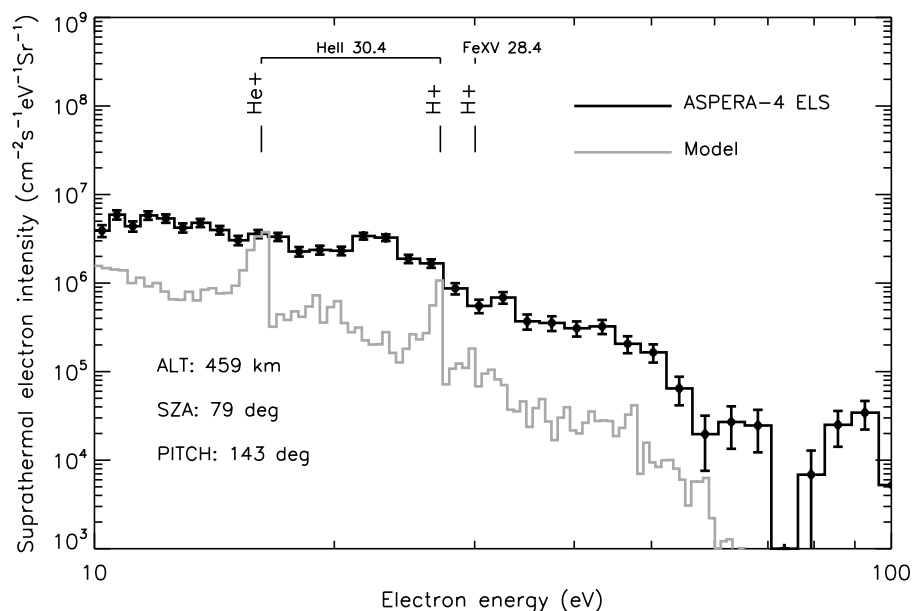


Figure 11. Similar to Figure 10 but at an altitude of 459 km.

straints on the magnetic field configuration near Venus. More specifically, the MAG-derived, slanted magnetic field configuration adopted in our kinetic model is probably realistic below ~ 350 km but oversimplified at higher altitudes in the sense that the actual magnetic field lines appear to be inclined more vertically.

5. Concluding Remarks

[31] Our model investigation was motivated by the recent report of *Coates et al.* [2008] on the VEx ASPERA-4 ELS observations of suprathermal electrons near Venus (made on 18 May 2006). Using a multistream, time-independent kinetic model, we compute the electron energy spectrum and compare our results to the observations. The input parameters include the VTS3 neutral atmosphere model of *Hedin et al.* [1983], the electron density and temperature models of *Theis et al.* [1984], as well as the TIMED/SEE level 3/4 solar spectrum obtained for the day of observation. Two magnetic field configurations are taken into account in this work, one with vertical magnetic field lines and the other adopted from the simultaneous VEx MAG measurements assuming a fixed magnetic field orientation. The vertical magnetic field case is used to discuss qualitatively the mechanisms that influence the suprathermal electron intensity as a function of altitude and energy. We focus on two specific questions. (1) What neutral species are associated with the various spectral peaks seen in the ASPERA-4 ELS data? (2) Are these spectral peaks produced in situ or alternatively, produced in deeper regions of the atmosphere followed by transport (along the magnetic field) to the site of observation? For quantitative data-model comparison, we consider both the vertical magnetic field case and the MAG-derived case.

[32] Distinct spectral features are clearly identified in the model spectra, most of which are associated with the ionization of various atmospheric neutral species (including CO_2 , O, He and H) by the strong HeII 30.4 nm solar line and an additional one associated with the ionization of CO_2 , O and/or H by the FeXV 28.4 nm solar line. By comparing the data with the model results, we identify the spectral peaks near 20 eV and 27 eV seen in the data as signatures of O ionization by HeII 30.4 nm photons to several electronic states ($^4\text{S}_0$, $^2\text{D}_0$ and $^2\text{P}_0$). We also identify another feature at ~ 11 eV as He ionization by the same photons.

[33] Using calculations, we confirm that the suprathermal electrons measured by ASPERA-4 ELS are not produced directly through in situ ionization, but instead are produced in deeper regions of the Venus atmosphere and transported along the magnetic field to the site of observation. The importance of transport can be illustrated in several ways.

[34] 1. Based on an analysis of the particle balance, we conclude that for suprathermal electrons with a representative energy of 20 eV, the atmospheric region below ~ 155 km is characterized by a local equilibrium between primary production and loss through collision with neutrals (including collisional ionization, dissociation and excitation). In that case, there is local electron energy deposition. Above ~ 250 km, loss of suprathermal electrons through transport is largely balanced by production through collision with neutrals.

[35] 2. Transport has a significant effect on the secondary electron production rate above ~ 160 km, though the details

rely on the assumed H density profile in the Venus upper atmosphere.

[36] 3. The suprathermal electron intensity is nearly isotropic near or below the ionospheric peak (at ~ 140 – 150 km [see *Cravens et al.*, 1981; *Fox*, 2007]) but becomes highly anisotropic at higher altitudes.

[37] We have presented a data-model comparison in terms of both the absolute magnitude of suprathermal electron intensity and the appearance of spectral peaks. A detailed quantitative comparison is limited due to the uncertainties in the neutral atmosphere model and/or the ambient magnetic field configuration, as well as the possible contribution of electron precipitation from the magnetized environment of Venus. Despite this, we find that below ~ 350 km, the model calculations with the MAG-derived, slanted magnetic field lines can reproduce the observations significantly more accurately than the case with vertical magnetic field lines. However, there is some disagreement at higher altitudes between the data and the model, namely, (1) the model intensities are significantly smaller than the measured values and (2) the model spectrum only presents signatures of H^+ and He^+ features, whereas the O^+ features present in the measured spectra are not seen. These findings help to put constraints on the magnetic field configuration near Venus. More specifically, the adopted magnetic field configuration appears to be overdraped, with the actual magnetic field lines probably penetrating deeper into the Venus atmosphere than we have assumed. Thus the analysis of photoelectron transport may provide useful information on the magnetic environment near planets, provided that the neutral atmosphere model is sufficiently well constrained. Calculations of suprathermal electron transport on Mars, which rely critically on the ambient magnetic field configuration, have been recently done by *Haider et al.* [2010].

[38] Since the magnetic field vector can only be measured along the VEx trajectory, complete information on the magnetic environment in our region of interest is not available to confirm our predictions of the magnetic field configuration near Venus. However, in follow-up studies, we will attempt to evaluate the suprathermal electron transport near Venus based on the magnetic field configuration derived from either magnetohydrodynamic [e.g., *Kallio et al.*, 1998] or hybrid [e.g., *Jarvinen et al.*, 2009] models.

Appendix A: Photon Impact and Electron Impact Cross Sections

[39] For completeness, we describe in this appendix the photon impact and electron impact cross-section data used for our kinetic model.

[40] The cross sections for photoionization of the atomic species (H, He and N) are evaluated with the analytic formulae given by *Verner et al.* [1996]. For O, we adopt the *Verner et al.* [1996] analytic results below 50 nm and the cross sections of *Angel and Samson* [1988] at higher wavelengths, combined with the branching ratio calculations of *Tayal* [2002]. We also consider the double photoionization of O, with the cross-section data taken from *Angel and Samson* [1988]. The N_2 dissociative photoionization and photoabsorption cross sections are adopted from *Stolte et al.* [1998], *Samson et al.* [1987] and *Chan et al.* [1993a]. For CO_2 , we consider both single and double dissociative photoionization

channels, with their cross sections taken from *Masuoka* [1994], *Hitchcock et al.* [1980] and *Siggel et al.* [1993]. The CO₂ photoabsorption cross sections are based on the work by *Chan et al.* [1993b]. For CO, we use the photoabsorption cross sections of *Chan et al.* [1993c], as well as the dissociative photoionization cross sections of *Masuoka and Nakamura* [1993], *Masuoka and Samson* [1981] and *Plummer et al.* [1977]. The photoabsorption and photoionization cross sections of H₂ are based on the work by *Chung et al.* [1993] and *Samson and Haddad* [1994].

[41] For electron impact processes, we consider both elastic and inelastic scattering, the latter of which includes electronic excitation, vibrational excitation, as well as dissociative ionization.

[42] The elastic scattering cross sections are based on the work by *LaBahn and Callaway* [1970], *Williams* [1975], *Blaħa and Davis* [1975], *Williams and Allen* [1989], *Bray et al.* [1991] and *Moyal and Salvat* [1997] for atomic species (H, He, N and O), *Sohn et al.* [1986], *García and Blanco* [2001] and *Itikawa* [2006] for N₂, *Itikawa* [2002] and *Morrison et al.* [1977] for CO₂, *Kanik et al.* [1992] for CO, as well as *Jain and Baluja* [1992] and *Brunger et al.* [1991] for H₂. For the electronic excitation of atomic species, we adopt the cross sections of *Stone et al.* [2002] for H and He, *Laher and Gilmore* [1990] for O, *Doering and Goemmel* [1991, 1992] and *Yang and Doering* [1996] for N. For electron impact ionization, the cross sections of *Bartlett and Stelbovics* [2004] are used for H, He and N, and those of *Laher and Gilmore* [1990] are used for O. For N₂, the dissociative ionization cross sections are taken from *Tian and Vidal* [1998b] and *Shemansky and Liu* [2005], while those for vibrational and electronic excitations from *Itikawa* [2006]. An additional process of neutral dissociation (N+N) is considered in our calculations, with the cross-section data taken from *Cosby* [1993]. The cross sections for electron impact dissociative ionization of CO₂ are based on the work by *Tian and Vidal* [1998a] and *Bhardwaj and Jain* [2009]. The CO₂ vibrational excitation cross sections are adopted from the compilations of *Itikawa* [2002] and *Kochem et al.* [1985]. Calculations of electronic excitation of CO₂ are based on the empirical expressions of *Jackman et al.* [1977], with the updated parameters given by *Bhardwaj and Jain* [2009]. Cross sections for CO electronic and vibrational excitations are based on the results of *Jackman et al.* [1977], *Brunger and Buckman* [2002] and *Poparić et al.* [2006]. We adopt the cross sections for electron impact dissociative ionization of CO from *Tian and Vidal* [1999] and *Mangan et al.* [2000]. Finally, the cross sections for dissociative ionization, electronic and vibrational excitation of H₂ are based on the work by *Straub et al.* [1996], *Brunger et al.* [1991], *Nishimura et al.* [1985] and *Khakoo and Trajmar* [1986]. The dissociative excitation of H₂ is considered as well, with cross sections taken from *Ajello et al.* [1991].

[43] **Acknowledgments.** We are grateful to Neville Shane for kindly providing the VEx ephemeris information on 18 May 2006 required for the kinetic modeling. We also wish to thank the Colorado TIMED/SEE group for making available to the community the solar irradiance data which we have used in the present study. This work was supported in part by the Science and Technology Facilities Council (STFC) rolling grant to Imperial College London. The VEx/ASPERA-4 work at MSSL-UCL was funded by STFC. I.M.-W. is funded by a University Research Fellowship of the Royal Society, UK. We also wish to thank the two anonymous referees, whose comments have significantly improved the quality of the paper.

[44] Robert Lysak thanks Thomas Cravens and another reviewer for their assistance in evaluating this paper.

References

- Ajello, J. M., D. E. Shemansky, and G. K. James (1991), Cross sections for production of H(*2p*, *2s*, *1s*) by electron collisional dissociation of H₂, *Astrophys. J.*, *371*, 422–431, doi:10.1086/169904.
- Angel, G. C., and J. A. R. Samson (1988), Total photoionization cross sections of atomic oxygen from threshold to 44.3 Å, *Phys. Rev. A*, *38*, 5578–5585, doi:10.1103/PhysRevA.38.5578.
- Barabash, S., et al. (2007), The Analyser of Space Plasmas and Energetic Atoms (ASPERA-4) for the Venus Express mission, *Planet. Space Sci.*, *55*, 1772–1792, doi:10.1016/j.pss.2007.01.014.
- Bartlett, P. L., and A. T. Stelbovics (2004), Electron-impact ionization cross sections for elements Z = 1 to Z = 54, *At. Data Nucl. Data Tables*, *86*, 235–265, doi:10.1016/j.adt.2003.11.006.
- Bhardwaj, A., and S. K. Jain (2009), Monte Carlo model of electron energy degradation in a CO₂ atmosphere, *J. Geophys. Res.*, *114*, A11309, doi:10.1029/2009JA014298.
- Blaħa, M., and J. Davis (1975), Elastic scattering of electrons by oxygen and nitrogen at intermediate energies, *Phys. Rev. A*, *12*, 2319–2324, doi:10.1103/PhysRevA.12.2319.
- Bray, I., D. A. Konovalov, and I. E. McCarthy (1991), Electron scattering by atomic hydrogen: Elastic and inelastic phenomena at 13.9–200 eV, *Phys. Rev. A*, *44*, 5586–5598, doi:10.1103/PhysRevA.44.5586.
- Brunger, M. J., and S. J. Buckman (2002), Electron-molecule scattering cross-sections: I. Experimental techniques and data for diatomic molecules, *Phys. Rep.*, *357*, 215–458, doi:10.1016/S0370-1573(01)00032-1.
- Brunger, M. J., S. J. Buckman, D. S. Newman, and D. T. Alle (1991), Elastic scattering and rovibrational excitation of H₂ by low-energy electrons, *J. Phys. B*, *24*, 1435–1448, doi:10.1088/0953-4075/24/6/027.
- Butler, D. M., and R. S. Stolarski (1978), Photoelectrons and electron temperatures in the Venus ionosphere, *J. Geophys. Res.*, *83*, 2057–2065, doi:10.1029/JA083iA05p02057.
- Chan, W. F., G. Cooper, R. N. S. Sodhi, and C. E. Brion (1993a), Absolute optical oscillator strengths for discrete and continuum photoabsorption of molecular nitrogen (11–200 eV), *Chem. Phys.*, *170*, 81–97, doi:10.1016/0301-0104(93)80095-Q.
- Chan, W. F., G. Cooper, and C. E. Brion (1993b), The electronic spectrum of carbon dioxide: Discrete and continuum photoabsorption oscillator strengths (6–203 eV), *Chem. Phys.*, *178*, 401–413, doi:10.1016/0301-0104(93)85079-N.
- Chan, W. F., G. Cooper, and C. E. Brion (1993c), Absolute optical oscillator strengths for discrete and continuum photoabsorption of carbon monoxide (7–200 eV) and transition moments for the X¹Σ⁺ → A¹Π system, *Chem. Phys.*, *170*, 123–138, doi:10.1016/0301-0104(93)80098-T.
- Chung, Y. M., E.-M. Lee, T. Masuoka, and J. A. R. Samson (1993), Dissociative photoionization of H₂ from 18 to 124 eV, *J. Chem. Phys.*, *99*, 885–889, doi:10.1063/1.465352.
- Coates, A. J., A. D. Johnstone, J. J. Sojka, and G. L. Wrenn (1985), Ionospheric photoelectrons observed in the magnetosphere at distances up to 7 Earth radii, *Planet. Space Sci.*, *33*, 1267–1275, doi:10.1016/0032-0633(85)90005-4.
- Coates, A. J., F. J. Crary, D. T. Young, K. Szego, C. S. Arridge, Z. Bebesi, E. C. Sittler Jr., R. E. Hartle, and T. W. Hill (2007), Ionospheric electrons in Titan's tail: Plasma structure during the Cassini T9 encounter, *Geophys. Res. Lett.*, *34*, L24S05, doi:10.1029/2007GL030919.
- Coates, A. J., et al. (2008), Ionospheric photoelectrons at Venus: Initial observations by ASPERA-4 ELS, *Planet. Space Sci.*, *56*, 802–806, doi:10.1016/j.pss.2007.12.008.
- Coates, A. J., S. M. E. Tsang, A. Wellbrock, R. A. Frahm, J. D. Winningham, S. Barabash, R. Lundin, D. T. Young, and F. J. Crary (2011), Ionospheric photoelectrons: Comparing Venus, Earth, Mars and Titan, *Planet. Space Sci.*, doi:10.1016/j.pss.2010.07.016, in press.
- Cosby, P. C. (1993), Electron-impact dissociation of nitrogen, *J. Chem. Phys.*, *98*, 9544–9553, doi:10.1063/1.464385.
- Cravens, T. E., T. I. Gombosi, J. Kozyra, A. F. Nagy, L. H. Brace, and W. C. Knudsen (1980), Model calculations of the dayside ionosphere of Venus: Energetics, *J. Geophys. Res.*, *85*, 7778–7786, doi:10.1029/JA085iA13p07778.
- Cravens, T. E., A. J. Kliore, J. U. Kozyra, and A. F. Nagy (1981), The ionospheric peak on the Venus dayside, *J. Geophys. Res.*, *86*, 11,323–11,329, doi:10.1029/JA086iA13p11323.
- Doering, J. P., and L. Goemmel (1991), Absolute differential and integral electron excitation cross sections for atomic nitrogen: I. The 4^sd⁰ → 3s⁴p (λ1200 Å) transition from 30 to 100 eV, *J. Geophys. Res.*, *96*, 16,021–16,024, doi:10.1029/91JA01462.

- Doering, J. P., and L. Goebel (1992), Absolute differential and integral electron excitation cross sections for atomic nitrogen: 2. The $4S^0 \rightarrow 2p^4\ ^4P$ ($\lambda 1135\ \text{\AA}$) transition from 30 to 100 eV, *J. Geophys. Res.*, *97*, 4295–4298, doi:10.1029/91JA03157.
- Doering, J. P., W. K. Peterson, C. O. Bostrom, and T. A. Potemra (1976), High resolution daytime photoelectron energy spectra from AE-E, *Geophys. Res. Lett.*, *3*, 129–131, doi:10.1029/GL0031003p00129.
- Fox, J. L. (2007), Near-terminator Venus ionosphere: How Chapman-esque?, *J. Geophys. Res.*, *112*, E04S02, doi:10.1029/2006JE002736.
- Fox, J. L., and A. Dalgarno (1979), Ionization, luminosity, and heating of the upper atmosphere of Mars, *J. Geophys. Res.*, *84*, 7315–7333, doi:10.1029/JA084iA12p07315.
- Fox, J. L., and K. Y. Sung (2001), Solar activity variations of the Venus thermosphere/ionosphere, *J. Geophys. Res.*, *106*, 21,305–21,336, doi:10.1029/2001JA000069.
- Fox, J. L., M. Galand, and R. E. Johnson (2008), Energy deposition in planetary atmospheres by charged particles and solar photons, *Space Sci. Rev.*, *139*, 3–62, doi:10.1007/s11214-008-9403-7.
- Frahm, R. A., et al. (2006a), Carbon dioxide photoelectron energy peaks at Mars, *Icarus*, *182*, 371–382, doi:10.1016/j.icarus.2006.01.014.
- Frahm, R. A., et al. (2006b), Locations of atmospheric photoelectron energy peaks within the Mars environment, *Space Sci. Rev.*, *126*, 389–402, doi:10.1007/s11214-006-9119-5.
- Frahm, R. A., et al. (2010), Estimation of the escape of photoelectrons from Mars in 2004 liberated by the ionization of carbon dioxide and atomic oxygen, *Icarus*, *206*, 50–63, doi:10.1016/j.icarus.2009.03.024.
- Galand, M., R. V. Yelle, A. J. Coates, H. Backes, and J.-E. Wahlund (2006), Electron temperature of Titan's sunlit ionosphere, *Geophys. Res. Lett.*, *33*, L21101, doi:10.1029/2006GL027488.
- Galand, M., L. Moore, B. Charnay, I. Mueller-Wodarg, and M. Mendillo (2009), Solar primary and secondary ionization at Saturn, *J. Geophys. Res.*, *114*, A06313, doi:10.1029/2008JA013981.
- Gan, L., T. E. Cravens, and M. Horanyi (1990), Electrons in the ionopause boundary layer of Venus, *J. Geophys. Res.*, *95*, 19,023–19,035, doi:10.1029/JA095iA11p19023.
- García, G., and F. Blanco (2001), Energy dependence of the total cross section for electron scattering by N_2 and CO molecules at energies above 1 keV, *Phys. Lett. A*, *279*, 61–66, doi:10.1016/S0375-9601(00)08822-7.
- Gustafsson, T., E. W. Plummer, D. E. Eastman, and W. Gudat (1978), Partial photoionization cross sections of CO_2 between 20 and 40 eV studied with synchrotron radiation, *Phys. Rev. A*, *17*, 175–181, doi:10.1103/PhysRevA.17.175.
- Haider, S. A., S. P. Seth, D. A. Brain, D. L. Mitchell, T. Majeed, and S. W. Bougher (2010), Modeling photoelectron transport in the Martian ionosphere at Olympus Mons and Syrtis Major: MGS observations, *J. Geophys. Res.*, *115*, A08310, doi:10.1029/2009JA014968.
- Hartle, R. E., T. M. Donahue, J. M. Grebowsky, and H. G. Mayr (1996), Hydrogen and deuterium in the thermosphere of Venus: Solar cycle variations and escape, *J. Geophys. Res.*, *101*, 4525–4538, doi:10.1029/95JE02978.
- Hedin, A. E., H. B. Niemann, W. T. Kasprzak, and A. Seiff (1983), Global empirical model of the Venus thermosphere, *J. Geophys. Res.*, *88*, 73–83, doi:10.1029/JA088iA01p00073.
- Hitchcock, A. P., C. E. Brion, and M. J. van der Wiel (1980), Absolute oscillator strengths for valence-shell ionic photofragmentations of N_2O and CO_2 (8–75 eV), *Chem. Phys.*, *45*, 461–478, doi:10.1016/0301-0104(80)87015-7.
- Hodges, R. R. (2000), Distributions of hot oxygen for Venus and Mars, *J. Geophys. Res.*, *105*, 6971–6982, doi:10.1029/1999JE001138.
- Itikawa, Y. (2002), Cross sections for electron collisions with carbon dioxide, *J. Phys. Chem. Ref. Data*, *31*, 749–767, doi:10.1063/1.1481879.
- Itikawa, Y. (2006), Cross sections for electron collisions with nitrogen molecules, *J. Phys. Chem. Ref. Data*, *35*, 31–53, doi:10.1063/1.1937426.
- Jackman, C. H., R. H. Garvey, and A. E. S. Green (1977), Electron impact on atmospheric gases: 1. Updated cross sections, *J. Geophys. Res.*, *82*, 5081–5090, doi:10.1029/JA082i032p05081.
- Jain, A., and K. L. Baluja (1992), Total (elastic plus inelastic) cross sections for electron scattering from diatomic and polyatomic molecules at 10–5000 eV: H_2 , Li_2 , HF, CH_4 , N_2 , CO, C_2H_2 , HCN, O_2 , HCl, H_2S , PH_3 , SiH_4 , and CO_2 , *Phys. Rev. A*, *45*, 202–218, doi:10.1103/PhysRevA.45.202.
- Jarvinen, R., E. Kallio, P. Janhunen, S. Barabash, T.-L. Zhang, V. Pohjola, and I. Sillanpää (2009), Oxygen ion escape from Venus in a global hybrid simulation: Role of the ionospheric O^+ ions, *Ann. Geophys.*, *27*, 4333–4348.
- Kallio, E., J. G. Luhmann, and J. G. Lyon (1998), Magnetic field near Venus: A comparison between Pioneer Venus Orbiter magnetic field observations and an MHD simulation, *J. Geophys. Res.*, *103*, 4723–4737, doi:10.1029/97JA02862.
- Kanik, I., J. G. Nickel, and S. Trajmar (1992), Total electron scattering cross section measurements for Kr, O_2 and CO, *J. Phys. B*, *25*, 2189–2196, doi:10.1088/0953-4075/25/9/022.
- Khakoo, M. A., and S. Trajmar (1986), Electron-impact excitation of the $a\ ^3\Sigma_g^+$, $B\ ^1\Sigma_g^+$, $c\ ^3\Pi_u$, and $C\ ^1\Pi_u$ states of H_2 , *Phys. Rev. A*, *34*, 146–156, doi:10.1103/PhysRevA.34.146.
- Knudsen, W. C., and K. L. Miller (1985), Pioneer Venus suprathermal electron flux measurements in the Venus umbra, *J. Geophys. Res.*, *90*, 2695–2702, doi:10.1029/JA090iA03p02695.
- Knudsen, W. C., K. Spenner, P. F. Michelson, R. C. Whitten, K. L. Miller, and V. Novak (1980), Suprathermal electron energy distribution within the dayside Venus ionosphere, *J. Geophys. Res.*, *85*, 7754–7758, doi:10.1029/JA085iA13p07754.
- Kochem, K.-H., W. Sohn, N. Hebel, K. Jung, and H. Ehrhardt (1985), Elastic electron scattering and vibrational excitation of CO_2 in the threshold energy region, *J. Phys. B*, *18*, 4455–4467, doi:10.1088/0022-3700/18/22/014.
- LaBahn, R. W., and J. Callaway (1970), Differential cross sections for the elastic scattering of 1 to 95 eV electrons from helium, *Phys. Rev. A*, *2*, 366–369, doi:10.1103/PhysRevA.2.366.
- Laher, R. R., and F. R. Gilmore (1990), Updated excitation and ionization cross sections for electron impact on atomic oxygen, *J. Phys. Chem. Ref. Data*, *19*, 277–305, doi:10.1063/1.555872.
- Lee, J. S., J. P. Doering, T. A. Potemra, and L. H. Brace (1980), Measurements of the ambient photoelectron spectrum from Atmosphere Explorer: I—AE-E measurements below 300 km during solar minimum conditions, *Planet. Space Sci.*, *28*, 947–971, doi:10.1016/0032-0633(80)90058-6.
- Lichtenegger, H. I. M., H. Gröller, H. Lammer, Y. N. Kulikov, and V. I. Shematovich (2009), On the elusive hot oxygen corona of Venus, *Geophys. Res. Lett.*, *36*, L10204, doi:10.1029/2009GL037575.
- Luhmann, J. G., and T. E. Cravens (1991), Magnetic fields in the ionosphere of Venus, *Space Sci. Rev.*, *55*, 201–274, doi:10.1007/BF00177138.
- Mangan, M. A., B. G. Lindsay, and R. F. Stebbings (2000), Absolute partial cross sections for electron-impact ionization of CO from threshold to 1000 eV, *J. Phys. B*, *33*, 3225–3234, doi:10.1088/0953-4075/33/17/305.
- Mantas, G. P., and W. B. Hanson (1979), Photoelectron fluxes in the Martian ionosphere, *J. Geophys. Res.*, *84*, 369–385, doi:10.1029/JA084iA02p00369.
- Masuoka, T. (1994), Single- and double-photoionization cross sections of carbon dioxide (CO_2) and ionic fragmentation of CO_2^+ and CO_2^{2+} , *Phys. Rev. A*, *50*, 3886–3894, doi:10.1103/PhysRevA.50.3886.
- Masuoka, T., and E. Nakamura (1993), Single-, double-, and triple-photoionization cross sections of carbon monoxide (CO) and ionic fragmentation of CO^+ , CO^{2+} , and CO^{3+} , *Phys. Rev. A*, *48*, 4379–4389, doi:10.1103/PhysRevA.48.4379.
- Masuoka, T., and J. A. R. Samson (1981), Dissociative and double photoionization of CO from threshold to 90 Å, *J. Chem. Phys.*, *74*, 1093–1097, doi:10.1063/1.441215.
- Mayol, R., and F. Salvat (1997), Total and transport cross sections for elastic scattering of electrons by atoms, *At. Data Nucl. Data Tables*, *65*, 55–154, doi:10.1006/adnd.1997.0734.
- McCormick, P. T., P. F. Michelson, D. W. Pettibone, and R. C. Whitten (1976), On the energy deposition of photoelectrons in the atmosphere of Venus, *J. Geophys. Res.*, *81*, 5196–5200, doi:10.1029/JA081i028p05196.
- Moore, L., M. Galand, I. Mueller-Wodarg, R. Yelle, and M. Mendillo (2008), Plasma temperatures in Saturn's ionosphere, *J. Geophys. Res.*, *113*, A10306, doi:10.1029/2008JA013373.
- Morrison, M. A., N. F. Lane, and L. A. Collins (1977), Low-energy electron-molecule scattering: Application of coupled-channel theory to $e-CO_2$ collisions, *Phys. Rev. A*, *15*, 2186–2201, doi:10.1103/PhysRevA.15.2186.
- Nagy, A. F., and T. E. Cravens (1988), Hot oxygen atoms in the upper atmospheres of Venus and Mars, *Geophys. Res. Lett.*, *15*, 433–435, doi:10.1029/GL015i005p00433.
- Nagy, A. F., J. P. Doering, W. K. Peterson, M. R. Torr, and P. M. Banks (1977), Comparison between calculated and measured photoelectron fluxes from Atmosphere Explorer C and E, *J. Geophys. Res.*, *82*, 5099–5103, doi:10.1029/JA082i032p05099.
- Nagy, A. F., T. E. Cravens, J.-H. Yee, and A. I. F. Steward (1981), Hot oxygen atoms in the upper atmosphere of Venus, *Geophys. Res. Lett.*, *8*, 629–632, doi:10.1029/GL008i006p00629.
- Nishimura, H., A. Danjo, and H. Sugahara (1985), Differential cross sections of electron scattering from molecular hydrogen: I. Elastic scattering and vibrational excitation ($X^1\Sigma_g^+$, $v = 0 \rightarrow 1$), *J. Phys. Soc. Jpn.*, *54*, 1757–1768, doi:10.1143/JPSJ.54.1757.

- Plummer, E. W., T. Gustafsson, W. Gudat, and D. E. Eastman (1977), Partial photoionization cross sections of N₂ and CO using synchrotron radiation, *Phys. Rev. A*, *15*, 2339–2355, doi:10.1103/PhysRevA.15.2339.
- Poparić, G. B., D. S. Belić, and M. D. Vikić (2006), Resonant vibrational excitation of CO by low-energy electrons, *Phys. Rev. A*, *73*, 062713, doi:10.1103/PhysRevA.73.062713.
- Reiser, G., W. Habenicht, K. Müller-Dethlefs, and E. W. Schlag (1988), The ionization energy of nitric oxide, *Chem. Phys. Lett.*, *152*, 119–123, doi:10.1016/0009-2614(88)87340-8.
- Robertson, I. P., et al. (2009), Structure of Titan's ionosphere: Model comparisons with Cassini data, *Planet. Space Sci.*, *57*, 1834–1846, doi:10.1016/j.pss.2009.07.011.
- Samson, J. A. R., and G. N. Haddad (1994), Total photoabsorption cross sections of H₂ from 18 to 113 eV, *J. Opt. Soc. Am. B*, *11*, 277–279, doi:10.1364/JOSAB.11.000277.
- Samson, J. A. R., T. Masuoka, P. N. Pareek, and G. C. Angel (1987), Total and dissociative photoionization cross sections of N₂ from threshold to 107 eV, *J. Chem. Phys.*, *86*, 6128–6132, doi:10.1063/1.452452.
- Shemansky, D. E., and X. Liu (2005), Evaluation of electron impact excitation of N₂ X ¹Σ_g⁺(0) into the N₂⁺ X ²Σ_g⁺(v), A ²Π_u(v), and B ²Σ_u⁺(v) states, *J. Geophys. Res.*, *110*, A07307, doi:10.1029/2005JA011062.
- Siggel, M. R. F., J. B. West, M. A. Hayes, A. C. Parr, J. L. Dehmer, and I. Iga (1993), Shape-resonance-enhanced continuum-continuum coupling in photoionization of CO₂, *J. Chem. Phys.*, *99*, 1556–1563, doi:10.1063/1.465324.
- Slavin, J. A., R. C. Elphic, C. T. Russell, F. L. Scarf, J. H. Wolfe, J. D. Mihalov, D. S. Intriligator, L. H. Brace, H. A. Taylor Jr., and R. E. Daniell Jr. (1980), The solar wind interaction with Venus: Pioneer Venus observations of bow shock location and structure, *J. Geophys. Res.*, *85*, 7625–7641, doi:10.1029/JA085iA13p07625.
- Sohn, W., K.-H. Kochem, K.-M. Scheuerlein, K. Jung, and H. Ehrhardt (1986), Near-threshold vibrational excitation and elastic electron scattering from N₂, *J. Phys. B*, *19*, 4017–4024, doi:10.1088/0022-3700/19/23/019.
- Solomon, S. C., S. M. Bailey, and T. N. Woods (2001), Effect of solar soft X-rays on the lower ionosphere, *Geophys. Res. Lett.*, *28*, 2149–2152, doi:10.1029/2001GL012866.
- Spenner, K., W. C. Knudsen, K. L. Miller, V. Novak, C. T. Russell, and R. C. Elphic (1980), Observation of the Venus mantle, the boundary region between solar wind and ionosphere, *J. Geophys. Res.*, *85*, 7655–7662, doi:10.1029/JA085iA13p07655.
- Spenner, K., W. C. Knudsen, and W. Lotze (1996), Suprathermal electron fluxes in the Venus nightside ionosphere at moderate and high solar activity, *J. Geophys. Res.*, *101*, 4557–4563, doi:10.1029/95JE03495.
- Spenner, K., Z. Dóbbé, A. F. Nagy, W. C. Knudsen, and W. Lotze (1997), Photoelectron fluxes in the Venus dayside ionosphere, *J. Geophys. Res.*, *102*, 2577–2583, doi:10.1029/96JA03341.
- Stolte, W. C., Z. X. He, J. N. Cutler, Y. Lu, and J. A. R. Samson (1998), Dissociative photoionization cross sections of N₂ and O₂ from 100 to 800 eV, *At. Data Nucl. Data Tables*, *69*, 171–179, doi:10.1006/adnd.1998.0775.
- Stone, P. M., Y.-K. Kim, and J. P. Desclaux (2002), Electron-impact cross sections for dipole- and spin-allowed excitations of hydrogen, helium, and lithium, *J. Res. Natl. Inst. Stand. Technol.*, *107*, 327–337.
- Straub, H. C., P. Renault, B. G. Lindsay, K. A. Smith, and R. F. Stebbings (1996), Absolute partial cross sections for electron-impact ionization of H₂, N₂, and O₂ from threshold to 1000 eV, *Phys. Rev. A*, *54*, 2146–2153, doi:10.1103/PhysRevA.54.2146.
- Szegő, K., Z. Dóbbé, W. C. Knudsen, A. F. Nagy, and V. D. Shapiro (1997), Energetic electrons in the dayside mantle of Venus, *J. Geophys. Res.*, *102*, 2175–2183, doi:10.1029/95JA03246.
- Tayal, S. S. (2002), Resonant photoionization cross sections and branching ratios for atomic oxygen, *Phys. Rev. A*, *65*, 032724, doi:10.1103/PhysRevA.65.032724.
- Theis, R. F., L. H. Brace, R. C. Elphic, and H. G. Mayr (1984), New empirical models of the electron temperature and density in the Venus ionosphere with application to transterminator flow, *J. Geophys. Res.*, *89*, 1477–1488, doi:10.1029/JA089iA03p01477.
- Tian, C., and C. R. Vidal (1998a), Single to quadruple ionization of CO₂ due to electron impact, *Phys. Rev. A*, *58*, 3783–3795, doi:10.1103/PhysRevA.58.3783.
- Tian, C., and C. R. Vidal (1998b), Electron impact ionization of N₂ and O₂: Contributions from different dissociation channels of multiply ionized molecules, *J. Phys. B*, *31*, 5369–5381, doi:10.1088/0953-4075/31/24/018.
- Tian, C., and C. R. Vidal (1999), Multiple ionization of CO due to electron impact, *Phys. Rev. A*, *59*, 1955–1965, doi:10.1103/PhysRevA.59.1955.
- Verner, D. A., G. J. Ferland, K. T. Korista, and D. G. Yakovlev (1996), Atomic data for astrophysics. II. New analytic fits for photoionization cross sections of atoms and ions, *Astrophys. J.*, *465*, 487–498, doi:10.1086/177435.
- Waite, J. H., Jr., T. E. Cravens, J. Kozyra, A. F. Nagy, S. K. Atreya, and R. H. Chen (1983), Electron precipitation and related aeronomy of the Jovian thermosphere and ionosphere, *J. Geophys. Res.*, *88*, 6143–6163, doi:10.1029/JA088iA08p06143.
- Williams, J. F. (1975), Electron scattering from hydrogen atoms: II. Elastic scattering at low energies from 0.5 to 8.7 eV, *J. Phys. B*, *8*, 1683–1692, doi:10.1088/0022-3700/8/10/018.
- Williams, J. F., and L. J. Allen (1989), Low-energy elastic scattering of electrons from atomic oxygen, *J. Phys. B*, *22*, 3529–3539, doi:10.1088/0953-4075/22/21/015.
- Woods, T. N., F. G. Eparvier, S. M. Bailey, P. C. Chamberlin, J. Lean, G. J. Rottman, S. C. Solomon, W. K. Tobiska, and D. L. Woodraska (2005), Solar EUV Experiment (SEE): Mission overview and first results, *J. Geophys. Res.*, *110*, A01312, doi:10.1029/2004JA010765.
- Yang, J., and J. P. Doering (1996), Absolute differential and integral electron excitation cross sections for atomic nitrogen: 3. The ⁴S⁰ → ²D(λ5200 Å) transition from 5 to 30 eV, *J. Geophys. Res.*, *101*, 21,765–21,768, doi:10.1029/96JA01944.
- Zhang, T.-L., et al. (2006), Magnetic field investigation of the Venus plasma environment: Expected new results from Venus Express, *Planet. Space Sci.*, *54*, 1336–1343, doi:10.1016/j.pss.2006.04.018.
- Zhang, T. L., et al. (2008), Initial Venus Express magnetic field observations of the magnetic barrier at solar minimum, *Planet. Space Sci.*, *56*, 790–795, doi:10.1016/j.pss.2007.10.013.

A. J. Coates, Mullard Space Science Laboratory, University College London, Holmbury St. Mary, Dorking RH5 6NT, UK.

J. Cui, National Astronomical Observatories, Chinese Academy of Sciences, A20 Datun Road, Beijing 100012, China. (cuij@nao.cas.cn)

M. Galand and I. C. F. Müller-Wodarg, Space and Atmospheric Physics Group, Department of Physics, Imperial College, Prince Consort Road, London SW7 2BW, UK.

T. L. Zhang, School of Earth and Space Sciences, University of Science and Technology of China, Hefei 230026, China.